Bioactive Materials 9 (2022) 461–474

Contents lists available at ScienceDirect

Bioactive Materials

journal homepage: www.sciencedirect.com/journal/bioactive-materials

Construction of multifunctional hydrogel based on the tannic acid-metal coating decorated MoS_2 dual nanozyme for bacteria-infected wound healing

Yang Li [a,b,c], Rongzhan Fu [a,b,c], Zhiguang Duan [a,b,c], Chenhui Zhu [a,b,c,*], Daidi Fan [a,b,c,**]

[a] Shaanxi Key Laboratory of Degradable Biomedical Materials, School of Chemical Engineering, Northwest University, Xi'an, 710069, Shaanxi, China
[b] Shaanxi R&D Center of Biomaterials and Fermentation Engineering, School of Chemical Engineering, Northwest University, Xi'an, 710069, Shaanxi, China
[c] Biotech. & Biomed. Research Institute, Northwest University, Xi'an, 710069, Shaanxi, China

ARTICLE INFO

Keywords:
MoS_2@TA/Fe nanozyme
Multifunctional hydrogel
POD-Like
CAT-Like
Anti-inflammation

ABSTRACT

Bacterial infection, tissue hypoxia and inflammatory response can hinder the infected wound repair process. To mitigate the above issues, tannic acid-chelated Fe-decorated molybdenum disulfide nanosheets (MoS_2@TA/Fe NSs) with dual enzyme activities were developed and anchored to a multifunctional hydrogel. The hydrogel exhibited excellent antibacterial ability owing to the combined effects of photothermal therapy (PTT), glutathione (GSH) loss, and the peroxidase (POD)-like activity (catalyse H_2O_2 into ·OH under acid condition) of MoS_2@TA/Fe NSs. Benefitting from the catalase (CAT)-like activity, the hydrogel could decompose H_2O_2 into O_2 at neutral pH to relieve hypoxia and supply adequate O_2. POD-like activity was mainly attributed to MoS_2 NSs, while CAT-like activity was primarily due to TA/Fe complex. Moreover, MoS_2@TA/Fe NSs endowed the hydrogel with outstanding anti-oxidant ability to scavenge redundant reactive oxygen species (ROS) and reactive nitrogen species (RNS) under neutral environment to maintain the balance of antioxidant systems and prevent inflammation. In addition, the hydrogel could inhibit the release of inflammatory factors for the anti-inflammatory property of TA. TA retained partial phenolic hydroxyl groups, which cross-linked the nanosheets to the network structure of the hydrogel and promoted the adhesion of hydrogels. Due to the dynamic boron ester bonds between polyvinyl alcohol (PVA), dextran (Dex), MoS_2@TA/Fe, and borax, the hydrogel demonstrated fast self-healing and rapid shape adaptability. This shape-adaptable adhesive hydrogel could fill the whole wound and closely contact the wound, ensuring that it achieved its functions with maximum efficiency. The MoS_2@TA/Fe nanozyme-anchored multifunctional hydrogel showed high potential for bacteria-infected wound healing.

1. Introduction

Infectious diseases caused by bacteria have been a growing health problem, resulting in millions of illnesses and deaths every year [1–3]. Bacterial infection-induced chronic skin defects are difficult to repair because the inflammatory response eventually causes cell death and tissue necrosis and reduces the process of wound repair [4,5]. Moreover, the above bacteria are extremely resistant to conventional antibiotics because of acquired resistance [6]. Additionally, there is less oxygen (O_2) in the wound with bacterial infection, which is not conducive to the repair of the wound. It has been proved that abundant O_2 can defend bacteria, accelerate cell proliferation and collagen synthesis, and promote tissue regeneration, which is a prerequisite for wound healing [7,8]. Therefore, the inhibition of both bacterial infection and excessive inflammation while supplying adequate O_2 are vital procedures for bacteria-infected wound treatments [9].

Hydrogels have been considered promising wound dressings because they can provide a moist environment, absorb wound exudates, and

Peer review under responsibility of KeAi Communications Co., Ltd.
* Corresponding author. Shaanxi Key Laboratory of Degradable Biomedical Materials, School of Chemical Engineering, Northwest University, Xi'an, 710069, Shaanxi, China.
** Corresponding author. Shaanxi Key Laboratory of Degradable Biomedical Materials, School of Chemical Engineering, Northwest University, Xi'an, 710069, Shaanxi, China.
E-mail addresses: zch2005@nwu.edu.cn (C. Zhu), faidaidi@nwu.edu.cn (D. Fan).

https://doi.org/10.1016/j.bioactmat.2021.07.023
Received 14 May 2021; Received in revised form 19 July 2021; Accepted 20 July 2021
Available online 26 July 2021

resist bacteria [10,11]. A satisfying hydrogel for infected chronic wound healing should possess the following advantages: fast self-healing to recover its original shape after damage [12,13], self-adhesiveness to attach to a wound site while keeping the wound moist [14,15], and rapid shape adaptability to ensure that the dressing completely fits the shape of the wound. Particularly, a shape-adaptable adhesive hydrogel can fill deep wounds and promote complete contact between the hydrogel and wound, achieving the function of the hydrogel with maximum efficiency. Therefore, a multifunctional hydrogel with antibacterial, anti-inflammatory and O_2 supplying activity is highly important for bacteria-infected wound defects [16–18].

Nanozymes have been widely explored to achieve better antibacterial efficiency due to their peroxidase (POD)-like activity. They can catalyse hydrogen peroxide (H_2O_2) into hydroxyl radicals (·OH), which possesses higher antibacterial activity and minimizes the toxicity of higher concentrations of H_2O_2 [19–21]. In particular, ·OH can cause initial oxidative lesions to the cell wall and membrane, and when combined with photothermal therapy (PTT), which is the conversion of near-infrared (NIR) light to induce hyperthermia, the deficiencies of each individual antibacterial model are overcome, thus showing enhanced antibacterial activities [22,23]. In addition, nanozymes with catalase (CAT)-like activity can decompose H_2O_2 into O_2 to relieve oxidative stress and replenish O_2, which is beneficial for wound healing [24–26].

Molybdenum disulfide (MoS_2), as a two-dimensional nanomaterial, possesses a large specific surface area, facile surface modification and good biocompatibility. The excellent absorption in the NIR range and the POD-like nanozyme properties of MoS_2 enable it to be applied in noninvasive antibacterial treatment methods [27–29]. Whereas, the CAT-like activity of MoS_2 is not high enough to generate adequate O_2 for wound. Tannic acid (TA) is a naturally occurring polyphenol extracted from plant sources and is considered an antioxidant, antimicrobial and anti-inflammatory agent [30]. TA/Fe, a new class of organic-inorganic hybrid material, presents excellent photothermal performance in the NIR region [31,32]. The PTT of TA/Fe complex has been widely researched, however, the nanozyme activity is few reported. Specifically, TA/Fe can convert H_2O_2 into O_2 to relieve hypoxia in wounds due to plentiful Fe (III). Therefore, the construction of MoS_2@TA/Fe nanocomplex is expected to highly and effectively kill microorganisms and provide O_2 for infected wound via the POD-like activity of MoS_2 and CAT-like activity of TA/Fe. More importantly, TA molecules present outstanding anti-inflammatory ability, inhibiting the inflammation induced by bacterial infection. Besides, MoS_2 and TA can scavenge free radicals at the wound site to regulate reactive oxygen species (ROS) and

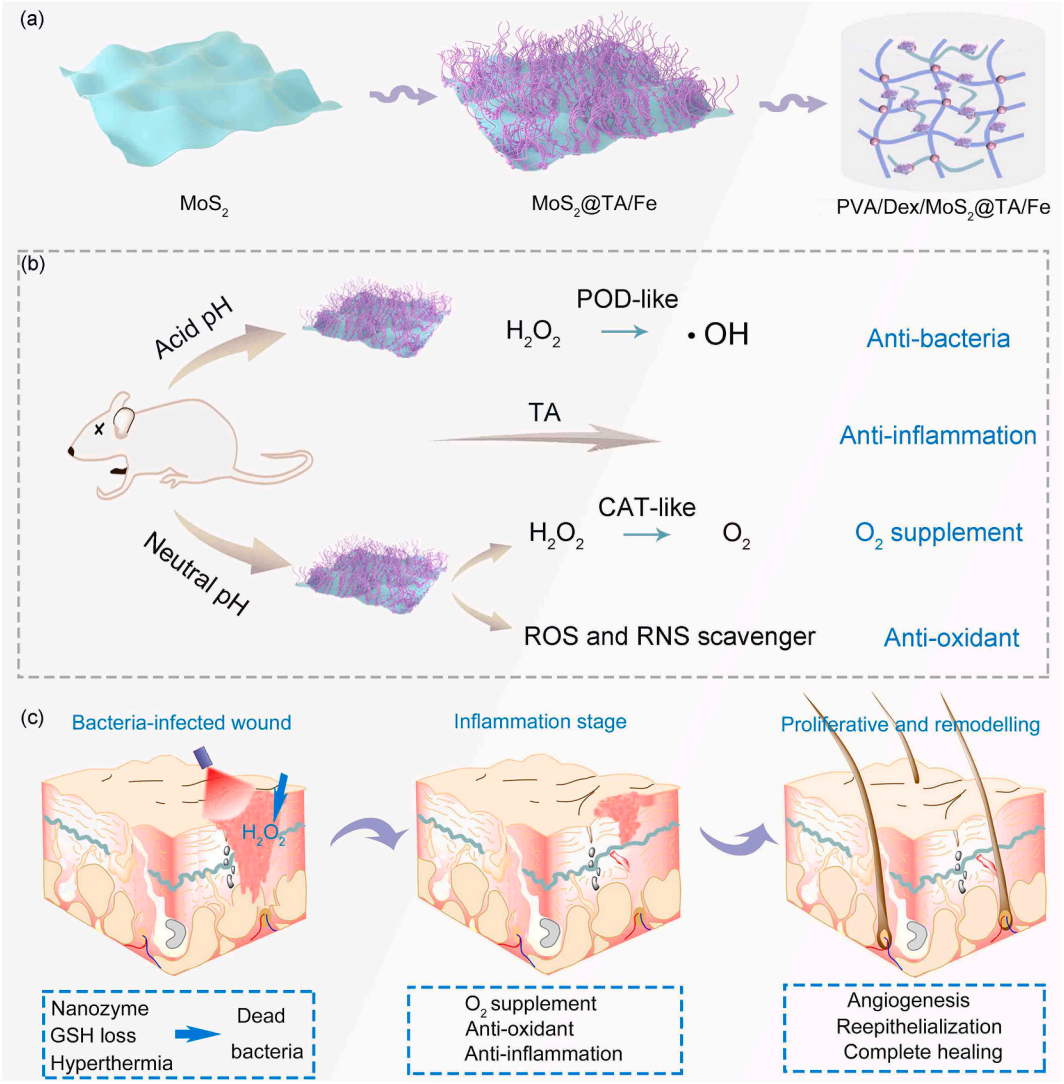

Scheme 1. (a) Schematic illustration of the preparation of the hydrogel; (b) dual enzyme activities of MoS_2@TA/Fe NSs; and (c) the mechanism of promoting wound repair.

reactive nitrogen species (RNS) levels based on the antioxidant system. Excessive free radical at the wound site will induce inflammatory response and have detrimental effects on wound healing [33]. Unfortunately, there have been no reports about MoS_2@TA/Fe NSs thus far, and few works on nanozyme-based multifunctional hydrogels that possess antibacterial, anti-oxidant, anti-inflammatory, and O_2 supply for bacteria-infected wound healing.

Herein, we developed an adhesive, self-healing, and shape-adaptable hydrogel for accelerating infected wound repair (Scheme 1). The multifunctional hydrogel was fabricated by dynamic boron ester bonds among MoS_2@TA/Fe NSs, polyvinyl alcohol (PVA), dextran (Dex), and borax, showing excellent antibacterial activity via PTT, glutathione (GSH) loss and POD-like activity under acid condition. Under neutral environment, the hydrogel demonstrated O_2 supply via its CAT-like ability, anti-oxidant property through scavenging ROS and RNS, and anti-inflammatory activity due to TA. By simultaneously eradicating infection, supplying O_2, eliminating free radical, and reducing inflammation, our hydrogel provided a sufficient microenvironment for cell proliferation, vascularization, granulation tissue formation and re-epithelialization, illustrating notably accelerated wound healing.

2. Experimental section

2.1. Synthesis of MoS_2@TA/Fe NSs

Briefly, 0.645 g of $Na_2MoO_4{\cdot}2H_2O$ and 0.813 g of CH_4N_2S were dissolved in 40 mL of deionized (DI) water. Then, the solution was transferred into a 50 mL Teflon-lined stainless steel autoclave, which was placed in an electric oven at 220 °C for 24 h. MoS_2 was collected by centrifugation at 8000 rpm for 3 min after the autoclave was cooled to room temperature, and the sediment was rinsed with DI water and ethanol three times. Finally, the MoS_2 powder was dried at 60 °C [34]. To obtain MoS_2@TA/Fe NSs, 100 mg of MoS_2 was dispersed in DI water and stirred for 10 min, then 2 mL of a TA solution (40 mg/mL) was added and stirred for 30 min. Afterwards, 2 mL of $FeCl_3{\cdot}6H_2O$ solution (10.6 mg/mL) was added, and the solution pH was adjusted to 7.5 with 1 M NaOH. The sediment was collected through three centrifugation cycles at 8000 rpm for 3 min to obtain MoS_2@TA/Fe NSs.

2.2. Fabrication of the MoS_2@TA/Fe incorporated PVA/Dex hydrogels

PVA and Dex were dissolved in DI water with concentrations of 8% and 3%, respectively. Then, MoS_2 and MoS_2@TA/Fe NSs (10 mg/mL) were added and sonicated for 10 min to achieve a uniform dispersion. Next, borax solution (2%) was added into the resultant solution to obtain the hydrogels (named PD, PDMo and PDMoT).

2.3. Characterization of MoS_2@TA/Fe NSs

The crystal structure of MoS_2@TA/Fe was measured by X-ray diffraction (XRD, Bruker D8 Advance). The morphology and microstructure of MoS_2@TA/Fe was determined by scanning electron microscopy (SEM, Hitachi, SU8010) and transmission electron microscopy-energy dispersive spectroscopy (TEM-EDS, FEI Talos F200X). The surface characteristic of MoS_2@TA/Fe was determined by X-ray photoelectron spectroscopy (XPS, Thermo Scientific Nexsa). The chemical structures were determined by Raman spectroscopy (Thermo Dxr 2Xi) and Fourier Transform Infrared (FTIR) spectroscopy (Nicolet Instrument Corporation, US) in the range of 400–4000 cm^{-1}.

2.4. Characterization of the MoS_2@TA/Fe-incorporated PVA/Dex hydrogels

The morphologies of the freeze-dried hydrogels were observed by SEM. The hydrogels were cut into two halves, placed in contact with each other and strengthened to investigate their self-healing ability. Moreover, their super-ductility was measured by placing three hydrogels at different positions and recording the flow process of the hydrogel. In addition, the hydrogels were recycled and reshaped into different shapes to examine their re-mouldability. The swelling capacity was conducted through weighing the dry hydrogel and the swollen hydrogel immersed in DI water for 24 h. The G′ and G″ were calculated under angular frequency from 0.1 to 100 rad/s to evaluate the viscoelasticity of the hydrogels.

2.5. POD-like activity characterization

The POD-like activity assays of hydrogels were evaluated through the oxidation of 3,3,5,5-tetramethylbenzidine (TMB) to oxTMB in a phosphate-buffered saline (PBS) solution (pH = 4.0). When the hydrogels were mixed with a TMB solution with and without H_2O_2, the UV–vis absorbance of the colour reaction (at 652 nm for oxTMB) was recorded at a certain time. To determine whether the POD-like activity of the PDMo and PDMoT hydrogels could decompose H_2O_2 to ·OH, different H_2O_2 (0, 50, 100, 200, 400, 600, and 800 μM) concentrations were tested. To further verify the effects of the NS concentration, temperature and pH on the POD-like activity of hydrogels, we sequentially added TMB and H_2O_2 into a PBS solution (pH = 4.0). The sample concentration, temperature, and pH were changed gradually from 0 to 25 mg/mL, 25–65 °C and 2.5–7, respectively. After reaction in the dark for 30 min, the absorbance of 100 μL of the mixture solution at 652 nm was tested. Three replicates were done for each group.

2.6. Detection of ·OH

Methyl violet (MV) was used as an indicator to measure the amount of generated ·OH. Briefly, the PDMo and PDMoT hydrogels were immersed in 5 mL of MV solution in the dark and reacted for 20 min. Then, the supernatant was collected and measured at 580 nm to detect ·OH production. In addition, after incubation in darkness for 10 min, the solution was irradiated at 808 nm for 10 min, and the absorbance was determined to evaluate the effect of the laser on nanozyme activity.

2.7. O_2 generation activity

To examine the O_2 generation ability of the PDMo and PDMoT hydrogels, 1 M H_2O_2 and the hydrogels were added to 20 mL of PBS (pH = 7.4), and then the O_2 concentration was recorded using a dissolved oxygen meter every 1 min.

2.8. Photothermal effects in vitro

The PD, PDMo and PDMoT hydrogel samples were exposed to 808 nm at a density of 1.0 W/cm^2 for 10 min. The temperature was recorded every 30 s by a thermal camera. The temperature changes were measured under different laser powers (1.0, 1.5, and 2.0 W/cm^2). In addition, the thermal stabilities of PDMo and PDMoT were tested through five laser on/off cycles.

2.9. Glutathione loss

The oxidation degree of GSH was assessed through Ellman's assay. Ellman reagent (5,5′-dithiobis (2-nitrobenzoic acid), DTNB) can oxidize thiol groups (−SH) to –S–S− producing a yellow product (2-nitro-5 thiobenzoate acid). In brief, 1 mL of a bicarbonate buffer solution (50 mM, pH = 8.7) containing the PD, PDMo and PDMoT hydrogel samples was mixed with 1 mL of a 0.8 mM GSH bicarbonate buffer solution in a 15 mL centrifuge tube and incubated at room temperature at a shaking speed of 150 rpm. Next, 1 mM of H_2O_2+GSH and GSH solutions were regarded as the positive and negative control groups, respectively. Afterwards, 3.5 mL of a 0.05 M Tris-HCl (pH = 8) solution and 670 μL of a bicarbonate buffer solution with 100 mM DTNB was added, and the

solution absorbance at 410 nm was recorded on a microplate spectrophotometer. Temperature-dependent GSH oxidation was performed through Ellman's assay in 20 and 40 °C water baths. NIR 808 nm laser-induced GSH oxidation was also evaluated. After the hydrogels were mixed with 0.8 mM GSH, the tubes were exposed to 808 nm irradiation for 20 min, and the temperature was maintained at 40 °C. The other steps were the same as above. The loss of GSH was calculated using the following equation: GSH loss (%) = OD (control) - OD (sample)/OD (control) × 100 %.

2.10. In vitro antibacterial experiment

E. coli and *S. aureus* solutions (1×10^5 CFU/mL) were divided into 14 groups: (1) Control, (2) PD hydrogel, (3) PDMo hydrogel, (4) PDMoT hydrogel, (5) PD + H_2O_2, (6) PDMo + H_2O_2, (7) PDMoT + H_2O_2, (8) Control + NIR, (9) PD + NIR, (10) PDMo + NIR, (11) PDMoT + NIR, (12) PD + NIR + H_2O_2, (13) PDMo + NIR + H_2O_2, and (14) PDMoT + NIR + H_2O_2. Then, 1 mL of a bacterial suspension was added to the hydrogel samples (prepared through 0.5 mL PVA/Dex solution) that were placed in 48-well culture plates. After incubation for 30 min, 100 μL of diluted bacteria were spread on an agar culture plate and incubated at 37 °C for 24 h. For groups treated with NIR, after incubation for 20 min, the hydrogels were further exposed to 808 nm irradiation (1.0 W/cm^2) for another 10 min. The next procedure was the same as that describe above. Afterwards, the bacteria were transferred onto silicon wafers, fixed with 4 % paraformaldehyde for 2 h at 12 °C, and dehydrated sequentially with 20, 40, 60, 80, and 100 % ethanol for 10 min. The dried bacteria were coated with gold for SEM.

2.11. Cytotoxicity assay and cell migration experiment

The *in vitro* cytotoxicity was measured by a standard 3-(4,5-dimethyl-2-thiazoLyl)-2,5-diphenyl tetrazolium bromide (MTT) assay. The culture medium extracts of different hydrogels were used to culture L929 cells instead of RPMI in 96-well plates. After co-incubation for 24, 48 and 72 h, 50 μL of MTT solution was added to each well, and the plate was incubated at 37 °C for 2 h. The absorbance at 490 nm of each well was measured to assess cell viability. Cells cultured with RPMI were used as controls, and the pure culture medium was considered the background. Here, the cell viabilities of H_2O_2 (100 μM) and ·OH (generated through NSs and H_2O_2) were also tested as above.

L929 cells were used to evaluate cell migration ability. The cells were seeded in 6-well plates at a density of 5–10 × 10^5 cells/well and cultured using complete growth medium with 10 % foetal bovine serum (FBS). Monolayer cells were formed after 16–24 h. A 10 μL pipette tip was used to scratch the monolayer cells. After removing cell debris, the hydrogel extract was added into the wells to contact the scratches. The group without hydrogel extract was the control. Cells in all groups were cultured with medium containing 0.1 % FBS for 20 h in a humidified incubator. It has been reported that medium containing 0.1 % FBS can inhibit cell proliferation and ensure that *in vitro* wound closure is only caused by cell migration. After incubation for 12 h, photos of the cell scratches were taken using an inverted fluorescence microscope (IX53, Olympus).

2.12. Construction of the LPS-stimulated macrophage model and treatment

The experimental group design was as follows: Control group, LPS group, and LPS + hydrogel extract groups. After LPS stimulation for 12 h, the hydrogel extracts were added to evaluate the anti-inflammatory ability of the hydrogels. Then, 24 h later, the cells were fixed with 4 % paraformaldehyde and calculated through immunofluorescence to assess the expression of proinflammatory factor (tumour necrosis factor-α, TNF-α) and anti-inflammatory cytokine (interleukin-10, IL-10). The anti-inflammation ability of TA molecule was also evaluated and the detailed procedure was as above.

2.13. Free radical scavenging experiment

1,1-diphenyl-2-picrylhydrazyl (DPPH), 2, 2′-azino-bis(3-ethylbenzothiazoline-6-sulfonic acid) (ABTS) and 2-Phenyl-4,4,5,5-tetramethylimidazoline-3-oxide-1-oxyl (PTIO) assays were carried out to evaluate the free radical scavenging ability. Regarding DPPH, 30 mg of the dried hydrogels were immersed in a DPPH solution (3 mL) in a dark environment at room temperature for 30 min. Finally, the absorbance was measured at 517 nm. The DPPH radical scavenging activity was measured as follows: Scavenging activity = (Ablank − Asample)/Ablank × 100 %. Here, Ablank refers to the absorbance of DPPH solution, and Asample is the absorbance of the DPPH solution after soaking the hydrogels for 30 min. Moreover, an ABTS assay was performed as follows. First, the ABTS radical cation ($ABTS^+$) was prepared by mixing a 7.4 mM ABTS solution with 2.6 mM potassium persulfate ($K_2S_2O_8$) in the dark at room temperature for 12 h. Then, the $ABTS^+$ solution was diluted to an absorbance of 0.70 ± 0.02 at 734 nm with DI water. Then, 30 mg of the hydrogels was added to 3 mL of the $ABTS^+$ solution and reacted in the dark for 20 min. The absorbance of the solution at 734 nm was recorded. The $ABTS^+$ scavenging activity was calculated using the following formula: Scavenging activity = (Ablank − Asample)/Ablank × 100 %, where Ablank and Asample are the absorbance of the $ABTS^+$ solution before and after mixing with samples, respectively. For the PTIO test, 3 mg of PTIO powder was dissolved in 20 mL of water, and the different hydrogel samples were added for 2 h at 37 °C to assess the free radical scavenging ability. The absorbance at 557 nm was tested and recorded. The DPPH, ABTS, and PTIO scavenging abilities of TA molecule were also tested as above.

2.14. Blood compatibility test

A haemolysis assay was carried out to determine the blood compatibility of the hydrogels. Specifically, 1 mL of fresh rabbit blood was diluted with 50 mL of PBS. The PD, PDMo and PDMoT hydrogels were placed into a tube containing 0.5 mL of physiological saline. Subsequently, 0.5 mL of diluted blood was added and incubated for 60 min at 37 °C. DI water and PBS were used as the positive and negative controls, respectively. Finally, all tubes were centrifuged at 1000 rpm for 10 min, and the absorbance of the supernatant was measured at 540 nm. The haemolysis ratio was calculated as follows: Haemolysis (%) = $[(OD_h - OD_n)/(OD_p - OD_n)] \times 100$ %, where OD_h, OD_n and OD_p are the absorbance values of the hydrogel samples, negative control (PBS) and positive control (DI water), respectively.

2.15. Animal wound healing test

An infectious skin defect model was carried out to evaluate the effects of photothermal and nanozyme therapy. All animal procedures were in accordance with protocols approved by the Institutional Animal Care committee. Briefly, female rats (250–300 g) were purchased from Xi'an Jiaotong University and divided into 14 groups: (1) Control, (2) PD hydrogel, (3) PDMo hydrogel, (4) PDMoT hydrogel, (5) PD + H_2O_2, (6) PDMo + H_2O_2, (7) PDMoT + H_2O_2, (8) Control + NIR, (9) PD + NIR, (10) PDMo + NIR, (11) PDMoT + NIR, (12) PD + NIR + H_2O_2, (13) PDMo + NIR + H_2O_2, and (14) PDMoT + NIR + H_2O_2. A wound of d = 8 mm was created in the dorsal area of the rat. The bacterial suspension of *S. aureus* (1×10^7 CFU/mL) was dropwise added to the wound area and treated with the different hydrogels. For the NIR-treated groups, the wound was exposed to 808 nm irradiation (1.0 W/cm^2) for 10 min. For nanozyme groups, 100 μM H_2O_2 was added. The wounds were photographed at days 0, 2, 5 and 8. Wound tissues were collected at day 2 and day 8 and fixed in 4 % paraformaldehyde for further analysis. HE staining, Giemsa staining and Masson's trichrome staining were carried out to evaluate the inflammatory response and collagen deposition.

Immunohistochemical analysis of TNF-α, IL-10 and vascular endothelial growth factor (VEGF) and immunofluorescence assays of VEGF and TNF-α were also carried out. In addition, the major organs, including the heart, liver, spleen, kidney and lung, were harvested and stained with HE at day 8.

2.16. Statistical analysis

All tests were repeated three or more times with triplicate samples and analysis of experimental data was carried out with SPSS software.

3. Results and discussions

3.1. Morphological and structural characterizations of MoS_2@TA/Fe NSs

The morphologies of MoS_2 and MoS_2@TA/Fe NSs were studied through SEM (Fig. S1). As shown in Fig. S1a, the MoS_2@TA/Fe nanosheets presented a rougher surface than MoS_2, which indicated the successful coating of TA/Fe. Fig. 1 shows the TEM images of MoS_2 and MoS_2@TA/Fe NSs. Wrinkled nanosheets with a few layers of stacked MoS_2 were shown in Fig. 1a. Some stripes were observed, and the lattice fringe of 0.66 nm corresponded to the (002) plane of MoS_2 (Fig. 1b). The high-angle annular dark-field scanning transmission electron microscopy (HAADF-STEM) and corresponding elemental mapping images of MoS_2 in Fig. 1c–f revealed the uniform distribution of the Mo and S elements. There were thin layers (TA/Fe) around the MoS_2 nanosheets (Fig. 1g), and an amorphous piece around the plane of MoS_2 was also observed (Fig. 1h). Fig. 1i-o shows the HAADF-STEM results and the corresponding elemental mapping images of MoS_2@TA/Fe, including Mo, S, C, O and Fe, demonstrating the synthesis of TA/Fe on the surface of MoS_2.

The elemental composition of MoS_2@TA/Fe was determined by XPS. The survey spectra indicated the presence of Mo, S, C, O and Fe elements (Fig. 2a). Fig. 2b shows the S 2p spectra of MoS_2@TA/Fe. The characteristic BEs of S $2p_{3/2}$ and S $2p_{1/2}$ at 162.1 and 163.3 eV, respectively, corresponded to the Mo–S bonds in MoS_2. The BEs of the Mo 3d signal of Mo $3d_{5/2}$ and Mo $3d_{3/2}$ at 229.3 and 232.3 eV, respectively, could be assigned to Mo(IV) in MoS_2 [35] (Fig. 2c). The C 1s spectrum was divided into three typical peaks. The major band centred at 284.6 eV was in accordance with C–C, and the other two bands at 281.6 and 288.9 eV were consistent with C–O and C═O species, respectively [36] (Fig. 2d). Fig. 2e shows the O 1s spectra of MoS_2@TA/Fe. The binding energies at 531.7 and 533.4 eV were attributed to the O–C/O–Fe and HO–C/HO–Fe species, respectively [37]. In the Fe 2p region, the characteristic peaks ascribed to Fe (II) $2p_{3/2}$ and Fe (III) $2p_{3/2}$ were observed at 709.7 and 712.0 eV, respectively [38,39] (Fig. 2f).

XRD, FTIR and Raman spectroscopies were utilized to characterize the crystalline features and chemical structures of MoS_2 and MoS_2@TA/Fe NSs. The XRD pattern further confirmed the formation of MoS_2, as evidenced by no other formed phases except for MoS_2 (Fig. 2g). The crystal diffraction pattern for MoS_2 could be well indexed to 2H–MoS_2 (JCPDS no. 37–1492) [40], while TA/Fe did not change the crystal structure of MoS_2. The FTIR spectra of MoS_2 and MoS_2@TA/Fe are shown in Fig. 2h. Compared with pure TA, the characteristic stretching bands between 1000 and 1800 cm^{-1} showed apparent shifts for MoS_2@TA/Fe, which may be due to the interaction of –OH with iron ions. The Raman spectra of MoS_2 and MoS_2@TA/Fe are shown in Fig. 2i. The two distinct bands at 379 and 405 cm^{-1} revealed the successful synthesis of MoS_2 [40]. In the MoS_2@TA/Fe NSs, a complex formed by the interaction between Fe(III) and TA was coated on the surface of

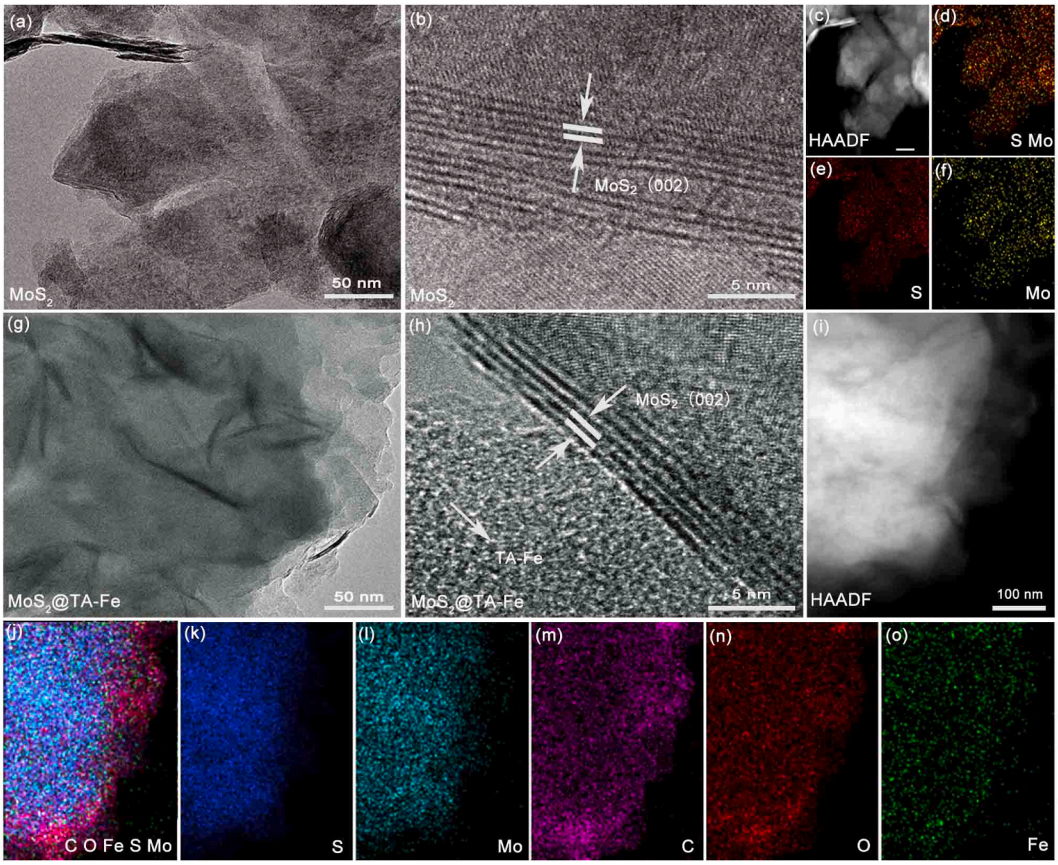

Fig. 1. (a, b) Low and high resolution TEM images of MoS_2 NSs. (c–f) HAADF-STEM image and corresponding elemental mappings of Mo and S in MoS_2 NSs. (g, h) Low- and high-resolution TEM images of MoS_2@TA/Fe NSs. (i–o) HAADF-STEM image and corresponding elemental mappings of Mo, S, C, O and Fe in MoS_2@TA/Fe NSs.

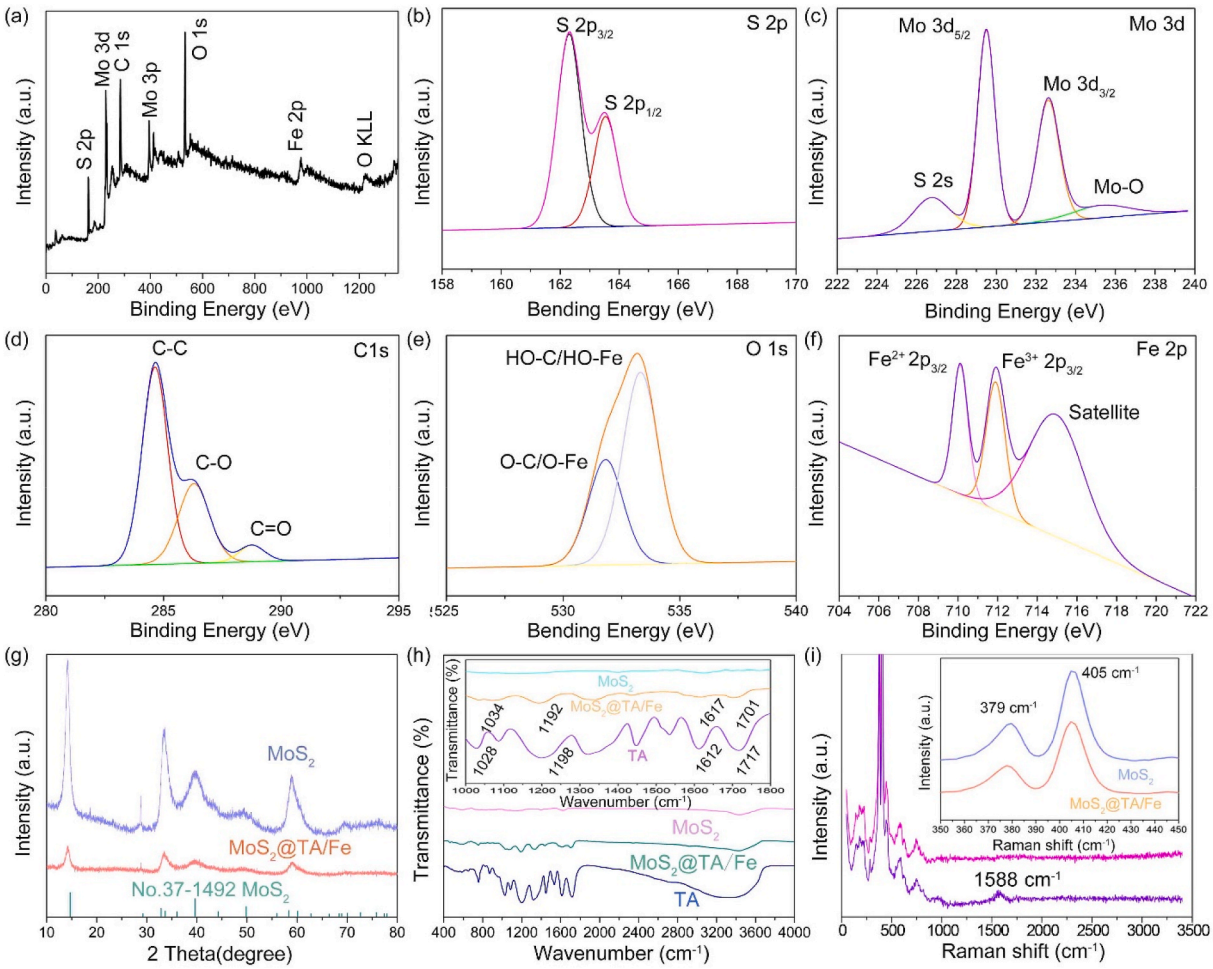

Fig. 2. (a–f) XPS survey spectrum and high-resolution XPS spectra of the S 2p, Mo 3d, C 1s, O 1s and Fe 2p signals for MoS_2@TA/Fe NSs. (g) XRD patterns, (h) FTIR spectra and (i) Raman spectra of MoS_2 and MoS_2@TA/Fe NSs.

MoS_2 NSs. Accordingly, the characteristic peak of the TA/Fe complex at 1588 cm^{-1} was observed. All the results indicated the successful formation of MoS_2@TA/Fe NSs.

3.2. Characterization of the hydrogels

In a typical experiment, the PDMoT hydrogel was prepared through physical hydrogen bond and chemical boron ester bond crosslinking (Fig. 3a). The boron ester bond can be dynamically associated and dissociated at room temperature, thereby providing the hydrogel with exceptional self-healing capacity [41,42]. This self-healing capacity was evaluated by a macroscopic test based on some small pieces. When being placed in a template, the pieces can integrate into a complete heart-shaped hydrogel. In addition, after a hydrogel was cut into two halves and then brought in contact at room temperature, the two halves can adhere to each other and bear its weight without breaking after 3s. Similarly, there was no breakage when stretching the healing hydrogel (Fig. 3b).

In Fig. 3c, it can be observed that the PDMoT hydrogel possessed fluidity, as three spherical hydrogels flowed into one hydrogel without cracking in 2 min, indicating that the hydrogel can adapt to the shape of the wound and fit tightly, especially when the body parts undergo frequent movements [41]. The PDMoT hydrogel could also be easily remoulded into various shapes, showing the free-forming properties of hydrogels, which is conducive to the use of hydrogels in various applications (Fig. 3d).

Boron ester bond and TA gave the hydrogel with an adhesive surface property, because the abundant alcohol and phenolic hydroxyl groups can bind with the organ tissues. Hydrogels that lack adhesiveness can fall off and cause inflammation. The hydrogels firmly adhered to various organic and inorganic surfaces, including skin, polytetrafluoroethylene (PTFE), glass, steel, and rubber (Fig. 3e). In addition, the hydrogel could adhere to fingers and elbows and did not fall off when bent from 0 to 90°. Thus, these hydrogels will have broad applications ranging from medical portable devices to tissue repair and wound dressings. As shown in Fig. S2, the microstructure of the cross-section of the freeze-dried PDMoT hydrogel was observed by SEM, showing a uniform interconnected porous structure with a pore size of approximately 3 μm that allowed gas exchange, thereby providing a comfortable and breathable environment for wounds.

It is well known that the hydrogel exhibits an elastic property in the region where G' is greater than G" and more liquid-like behaviour when G" is greater than G' [44]. The intersection between the G' and G" curves was a typical behaviour of structured fluids that possessed both entangled chains and reversible cross-links. As shown in Fig. S3, PD, PDMo, and PDMoT hydrogels all presented both fluid and solid behaviour, especially the excellent fluidity, which was conducive to the shape-adaptivity of the hydrogels to fit the cavity of different wounds.

Swelling ratio is a vital index to evaluate the wound dressing. From Fig. S4, the swelling value of the PD and PDMo hydrogels were 558 % and 543 %, respectively. PDMoT hydrogel had a better swelling capacity (769 %), due to the decline in crosslinking density. All the hydrogels presented satisfying swelling ability, suitable for quickly absorbing tissue fluid and effectively preventing suppuration.

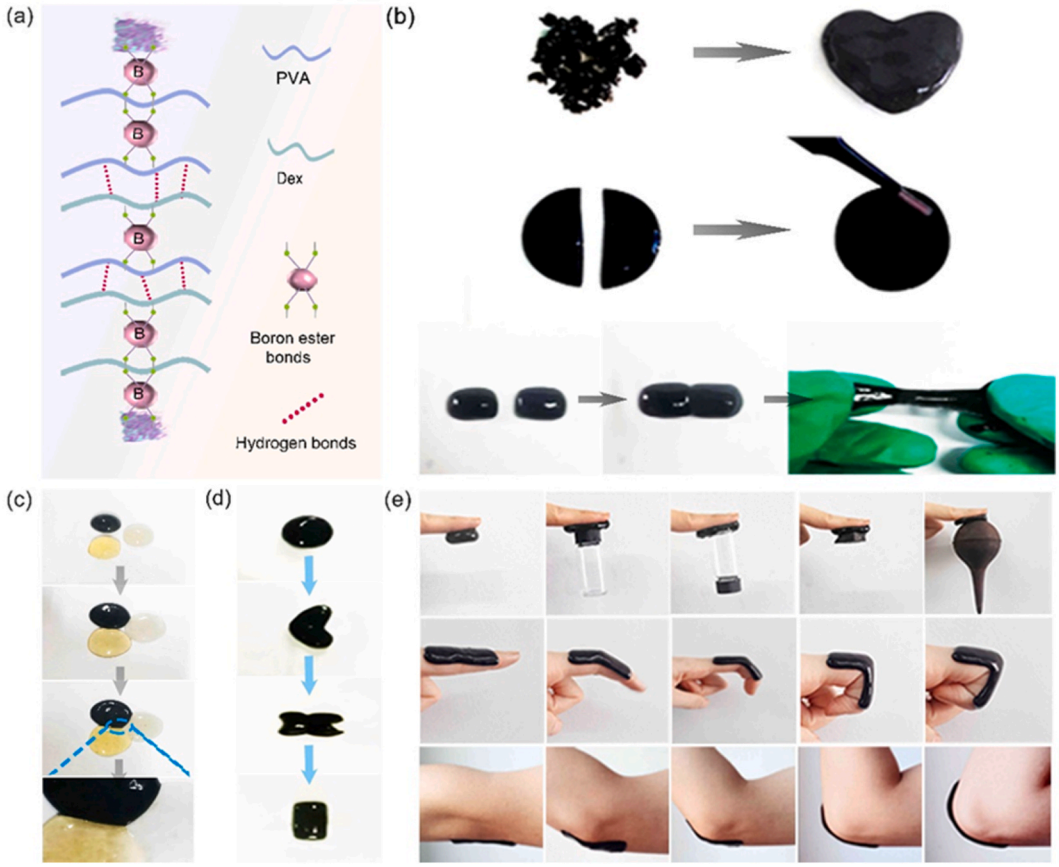

Fig. 3. (a) Hydrogel crosslinking mechanism diagram; (b) self-healing; (c) super-ductility; (d) re-mouldability; and (e) adhesion on different substrate, fingers and elbows.

3.3. Investigation of the POD-like property

The POD-like catalytic activity of the PDMoT hydrogel could kill bacteria efficiently, and was determined through the TMB colorimetric detection method [42]. Briefly, nanozymes could oxidize colourless TMB to the blue oxide of TMB (oxTMB) with an absorbance peak at 652 nm in the presence of H_2O_2. In Fig. 4a, the PDMo and PDMoT hydrogels could catalyse the oxidation of TMB, and a blue colour was observed after reaction for 5 min. Moreover, the catalytic activity was proven to be dependent on the NSs contents, H_2O_2 concentrations, pH values, and temperature. The absorbance value increased with an increasing concentration of MoS_2 and MoS_2@TA/Fe (0, 2, 5, 10, 15, 20, 25 mg/mL) (Fig. 4b) and an increasing concentration of H_2O_2 (0, 50, 100, 200, 400, 600, 800 μM) (Fig. 4c); the results were consistent with the colour changes of the solutions. Moreover, pH values ranging from 2.5 to 7 versus the catalytic activities of the PDMo and PDMoT hydrogels were determined (Fig. 4d). The relatively higher POD-like activities of the PDMo and PDMoT hydrogels occurred in the acidic pH value range of 2.5–5.0. In addition, the POD-like activities of the two hydrogels also depended on the temperature (Fig. 4e), and relatively higher catalytic activities were displayed from 25 to 55 °C, at which point, the hydrogel would continuously and efficiently catalyse the generation of ·OH to kill bacteria *in vivo*. Particularly, the absorbance at 652 nm in the PDMoT group was slightly higher than that in the PDMo hydrogel, which demonstrated that the POD-like activity was mainly due to MoS_2 NSs.

3.4. ROS detection

The content of ·OH was detected by MV using UV–vis spectrophotometry. After ·OH reacts with MV in an acidic environment, the colour of MV will fade, and the absorbance peak at 580 nm will decrease. As shown in Fig. 4f, a decreasing peak intensity was observed in the presence of MoS_2 and MoS_2@TA/Fe, which demonstrated the generation of ·OH. In addition, after irradiation at 808 nm for 10 min, the absorbance peak at 580 nm disappeared (Fig. 4g), suggesting that the nanozyme activity of MoS_2@TA/Fe NSs could be enhanced under NIR irradiation.

3.5. CAT-like performance

CAT-like activity of nanozyme can decompose H_2O_2 into O_2 under neutral conditions. Fig. 4h shows the O_2 generation content at different time when mixed different hydrogels with H_2O_2. The O_2 concentration did not change for PS hydrogels and maintained at 7.67 mg/L. However, the O_2 content increased over time and reached 14.5 mg/L for the PDMo hydrogels and 25.8 mg/L for the PDMoT hydrogels, showing that TA/Fe coating contributed much more CAT-like activity to generate O_2. Therefore, the TA/Fe complex made up for the deficiency of CAT-like activity of MoS_2 nanozyme. Fig. 4i clearly demonstrates the POD-like and CAT-like properties of the hydrogels.

3.6. Photothermal investigation of the hydrogels

The photothermal effects of the hydrogels were evaluated by monitoring the temperature change with various concentrations of MoS_2 and MoS_2@TA/Fe with an 808 nm laser (1.0 W/cm^2). As shown in Fig. 5a, a negligible temperature change could be seen for the PD hydrogel when irradiated for 10 min. However, remarkable temperature increases were recorded for the different concentrations of MoS_2 and MoS_2@TA/Fe. It was evident that MoS_2@TA/Fe NSs presented better photothermal results than MoS_2 NSs. The maximum temperature of the hydrogels increased with an increasing NS concentration. Fig. 5b presents the temperature changes of hydrogels under various laser powers. With the

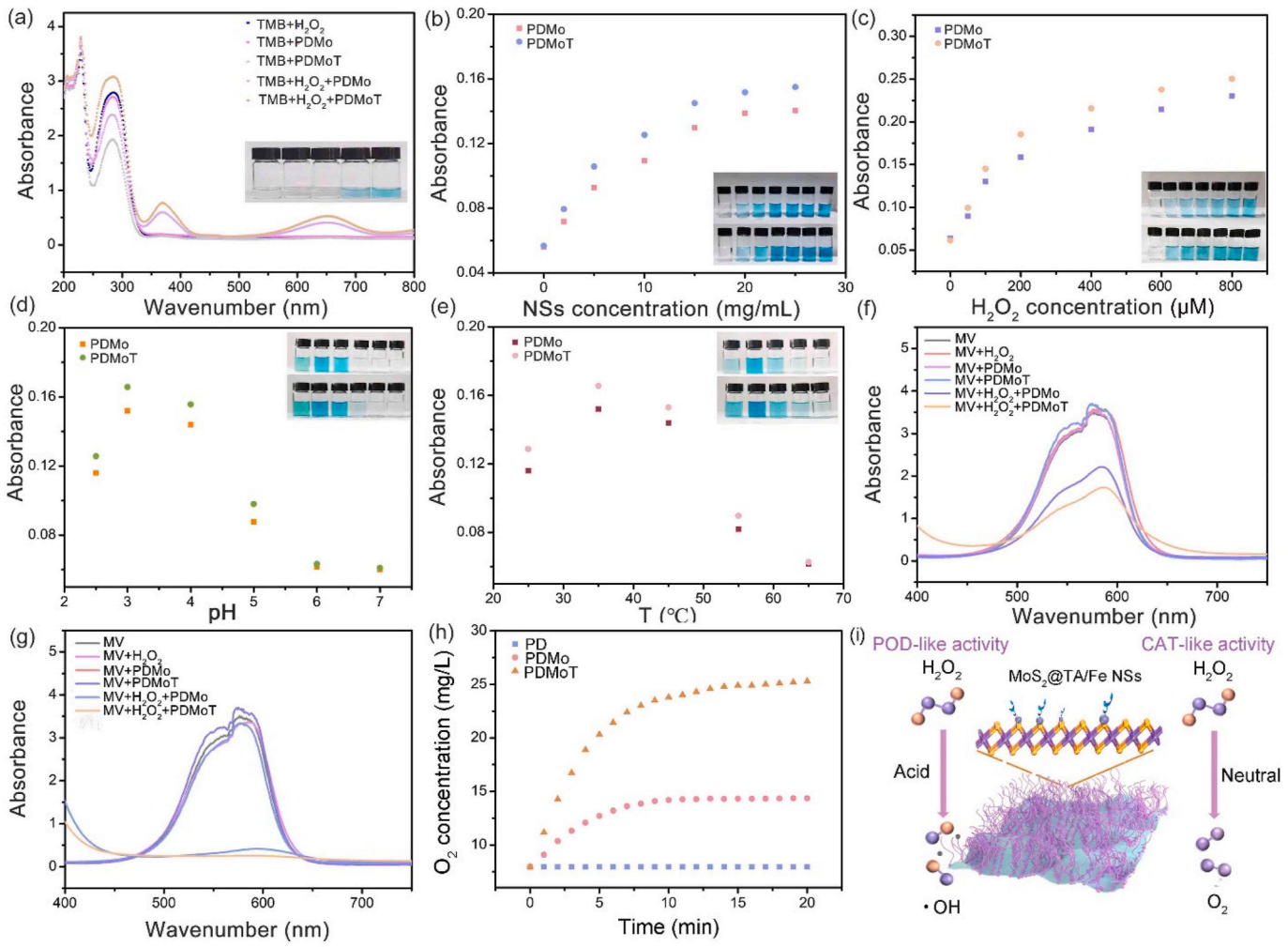

Fig. 4. (a) UV–vis absorbance spectra of solutions containing TMB, H_2O_2, and the different hydrogels in PBS. (b) MoS_2 and MoS_2@TA/Fe NSs concentration-dependent POD-like activity. (c) H_2O_2 concentration-dependent POD-like activity. (d) pH-dependent POD-like activity. (e) Temperature-dependent POD-like activity. (f) ·OH detected from the degradation of MV without an 808 nm laser. (g) ·OH detected from the degradation of MV irradiated at 808 nm. (h) O_2 generation activity detection. (i) Schematic diagram of the POD- and CAT-like activities of MoS_2@TA/Fe NSs.

increase of laser power, PDMoT hydrogels showed better photothermal conversion ability. To calculate the photostability of the PDMoT hydrogels, cyclical irradiation at 808 nm was carried out. From Fig. 5c, the PDMoT hydrogels demonstrated excellent photostability.

3.7. GSH oxidation level

GSH plays an important role in the bacterial antioxidant defence system because it can protect cellular components from damage induced by oxidative stress [43,44], which in bacteria can significantly weaken the bactericidal effect of POD-like nanomaterials [44]. To ensure the antibacterial ability of nanozymes, the loss of GSH is essential. Here, Ellman's assay was carried out to measure GSH loss. Fig. 5d indicates that GSH oxidation was temperature- and time-independent. In particular, the GSH at 40 °C was greater than that at 20 °C. In Fig. 5e, GSH oxidation has concentration-dependent properties. As the concentration of MoS_2 and MoS_2@TA/Fe NSs increased, GSH oxidation increased, demonstrating that MoS_2 could accelerate the oxidation of organic thiols (R–SH) to yield disulfides (R–S–S−R). Fig. S5 presents corresponding photographs of the colour change after GSH treatment with different concentrations of MoS_2 and MoS_2@TA/Fe NSs. A lighter colour marked greater GSH loss. Fig. 5f and Fig. S6 compares the GSH loss at 40 °C under 808 nm NIR irradiation and in water bath, illustrating that the GSH loss under NIR was much higher than that at the same temperature in a water bath. Therefore, NIR irradiation could facilitate the loss of GSH and enhance the antibacterial ability of the material. The possible antibacterial mechanism of the PDMoT hydrogels was the synergistic effects among the hyperthermia, generation of ·OH, and GSH oxidation.

3.8. In vitro antibacterial efficiency assessment

The antibacterial properties of the hydrogels for *E. coli* and *S. aureus* were assessed by the classical plate count method (Fig. 6). Compared to the control and PD groups, the PDMo, PDMoT and PD+H_2O_2 groups presented slight antibacterial effects. The PDMo+H_2O_2 and PDMoT+H_2O_2 groups showed better antibacterial effects than the other groups even without NIR irradiation, which was due to the nanozyme activity of MoS_2 and MoS_2@TA/Fe NSs. After 808 nm laser irradiation for 10 min, the PDMo and PDMoT groups exhibited enhanced antimicrobial ability when compared with that without NIR. The temperature of the PDMo and PDMoT hydrogels after 10 min illumination was 40.2 °C and 43.3 °C, respectively, which cannot cause any damage on normal human tissues. In particular, the PDMoT+H_2O_2+NIR groups demonstrated the best antibacterial ability (an inhibition rate of up to nearly 100 % on both *E. coli* and *S. aureus*), owing to the combined effects of the POD-like activity of MoS_2@TA/Fe to generate ·OH, GSH loss and the hyperthermia induced by MoS_2@TA/Fe, followed by the PDMo+H_2O_2+NIR group. To further explain the antibacterial ability,

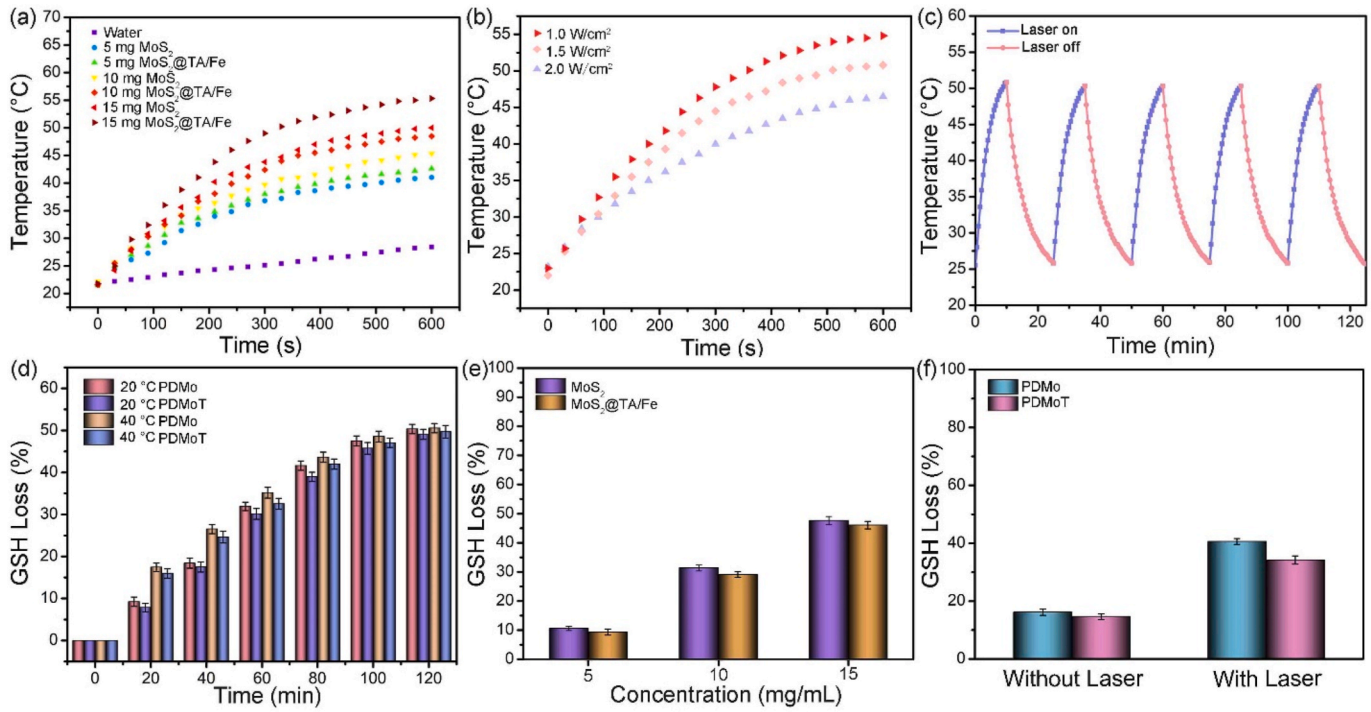

Fig. 5. (a) Temperature changes of the hydrogels containing MoS_2 and MoS_2@TA/Fe NSs irradiated by an 808 nm NIR laser (1.0 W/cm^2). A PD hydrogel acted as a control. (b) Temperature changes of the PDMoT hydrogels at different laser powers. (c) Thermal stabilities of the PDMoT hydrogels during five on/off cycles. (d) Loss percentage of GSH after incubation at 20 and 40 °C in a water bath at different time. (e) GSH loss after incubation with hydrogels containing different MoS_2 and MoS_2@TA/Fe NSs concentrations. (f) Loss percentage of GSH after incubation with and without NIR laser irradiation.

SEM images were taken to investigate *E. coli* and *S. aureus* after irradiation. *E. coli* was rod-shaped, and *S. aureus* was spherical with a smooth surface for the control and PD groups. Regarding the PD+H_2O_2+NIR, PDMo+NIR and PDMoT+NIR groups, a few disruptions could be seen on cell walls at 808 nm, indicating that H_2O_2 or light alone had only a limited influence on the integrity of cell walls. Whereas, the cell walls of bacteria became completely wrinkled and even fractured after the treatment of NIR and nanozyme, demonstrating that this synergistic treatment might exhibit a stronger antibacterial ability.

3.9. In vitro cell and blood compatibility of hydrogels

The cell biocompatibility of the hydrogels was evaluated by MTT assay and live/dead staining. The cells treated with PD, PDMo and PDMoT hydrogels all presented a normal morphology at day 1 (Fig. 6e), and the cells treated with the PD hydrogel exhibited a proliferation trend when compared with the control group because Dex as a polysaccharose could promote cell proliferation. In particular, the PDMo and PDMoT hydrogel groups presented higher cell viabilities than the PD group (Fig. 6f) because MoS_2 could promote L929 cell proliferation. Therefore, the hydrogels could promote the growth of L929 cells, which would play a vital role in the wound healing process. In our experiment, H_2O_2 was introduced to generate ·OH only at the first day during the treatment to kill the bacteria in a short time. The viabilities of cells treated with H_2O_2 and generated ·OH were tested and shown in Fig. S7. Although H_2O_2 (100 μM) and generated ·OH had a negative impact on L929 cell growth, they would not cause any great damage for the normal tissues, which were proved by the results of animal experiment (Fig. 8). Instead, the wound healing rate can be notably accelerated after the treatment of nanozyme therapy. The migration of cells was recorded at 0 and 12 h (Fig. S8). The hydrogel groups all had effects on cell mobility. The relative wound areas of the PD, PDMo and PDMoT groups were smaller than those of the blank group because Dex and MoS_2 could promote cell migration.

Furthermore, the blood compatibility of the hydrogels was evaluated with red blood cells using pure water as the positive control. The results demonstrated that there was negligible haemolytic activity for all the experimental groups (Fig. 6g). Fig. S9 tests the haemolytic ratio of MoS_2 and MoS_2@TA/Fe NSs, and the results illustrated a good blood compatibility. Therefore, it was considered that the hydrogels presented excellent cell and blood compatibility and would be safe as dressings for further *in vivo* application.

3.10. In vitro anti-inflammation and antioxidant assays

To further explore the mechanism of the effect of hydrogels on inflammation, we constructed a LPS-stimulated macrophage model *in vitro* and detected the levels of TNF-α and IL-10. As shown in Fig. 6h, the expression of the inflammatory cytokine TNF-α was significantly increased in the LPS group, while it was decreased in the PDMoT group. However, the anti-inflammatory cytokine IL-10 was significantly upregulated in the PDMoT group compared with the LPS group, indicating the remarkable anti-inflammatory effect of TA during nanozyme therapy for bacteria-infected wounds. Additionally, the anti-inflammation ability of TA *in vitro* was evaluated. From Fig. S10a, TA can inhibit the expression of TNF-α, and promote the expression of IL-10, demonstrating the excellent anti-inflammation capacity of TA.

In addition, the hydrogel could eliminate free radicals under neutral conditions. Excessive RNS and ROS could interfere with signaling cascades and destroy cells and tissues. DPPH and ABTS are typical nitrogen free radicals, which are widely applied as model molecules to assess the RNS scavenging ability of materials. PTIO is the typical oxygen free radicals and used in the evaluation of ROS scavenging capacity. Fig. 7a, d and g presents the mechanism of DPPH, ABTS and PTIO redox reaction, respectively. Fig. 7b shows the absorption curves of a DPPH radical solution before and after exposure to hydrogels. When DPPH was exposed to the PDMo and PDMoT hydrogels, the absorption peak at 517 nm became weak, and the colour of the solution became a deep yellow.

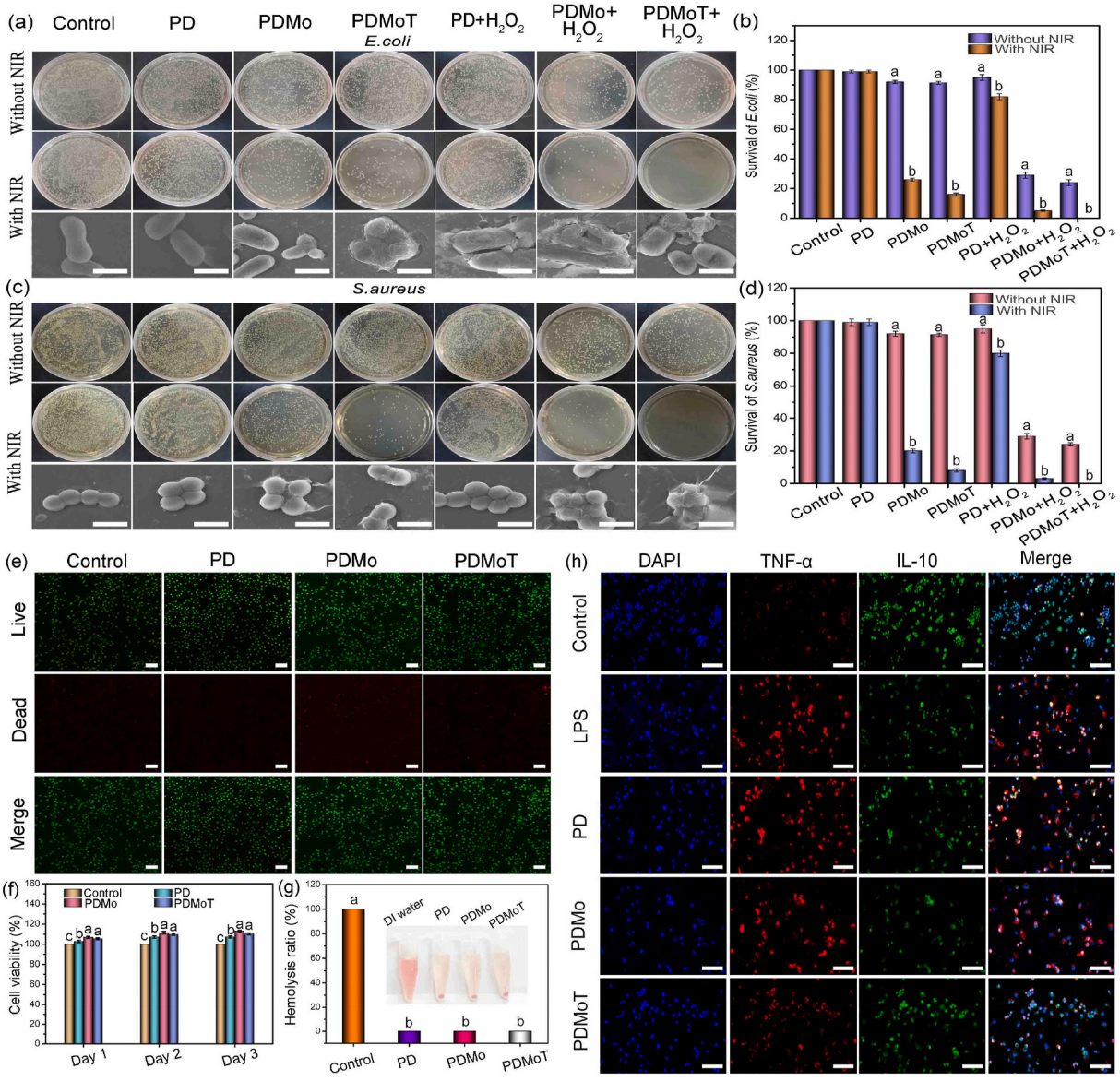

Fig. 6. Photographs of the bacterial colonies of (a) *E. coli* and (c) *S. aureus* and the corresponding SEM images in groups with NIR. The scale bar is 2 μm. Relative bacterial viabilities of *E. coli* (b) and *S. aureus* (d) determined by the plate count method. (e) Images of the live/dead staining of L929 cells after co-culture with different hydrogel extracts. (f) Cell viability of the hydrogels at days 1, 2 and 3. The scale bar is 100 μm. (g) Haemolysis ratio of the hydrogels. (h) TNF-α and IL-10 expression in different groups after co-culture with LPS-induced macrophages. The scale bar is 50 μm.

Fig. 7c illustrates that as the concentration of MoS_2 and MoS_2@TA/Fe increased, the hydrogel exhibited a higher DPPH scavenging ratio. Fig. 7e and f shows the scavenging ability of the hydrogels against $ABTS^+$. The two hydrogel hydrogels all showed certain $ABTS^+$ scavenging ability, and the colour shifted to a light blue. PTIO assay was also carried out to evaluate its ability to scavenge oxygen free radical. From Fig. 7h and i, MoS_2@TA/Fe possessed better PTIO scavenging ability than MoS_2. There was weaker absorbance peak at 557 nm. These results demonstrated that the PDMoT hydrogel presented great anti-oxidation capacity, which was attributed to the combined effects of MoS_2 and TA. The hydrogel was expected to eliminate the ROS and RNS at the wound site under neutral condition to maintain the balance of anti-oxidant system and promote skin regeneration. The anti-oxidant property of TA was also examined and shown in Fig. S10 (b-d), demonstrating that TA had a good ability of scavenging RNS and ROS.

3.11. Wound healing evaluation and histopathological evaluation in vivo

Encouraged by the excellent capability for bacterial inhibition, anti-oxidant, and anti-inflammatory ability of the PDMoT hydrogel, a *S. aureus* infected skin defect model on the back of a rat was established to assess the wound healing process of hydrogels. The treatment strategy was shown in Fig. 8a, and the healing capabilities and wound closure processes (Fig. 8b and Fig. S11) in all groups were recorded for a detailed analysis.

Wound infection is one of the major causes of death of injured patients, therefore, the effects of the hydrogels in preventing infection were assessed through immunohistochemistry analysis of the secretion of typical proinflammatory factors TNF-α in the wound [45] (Fig. 8c). Large amounts of TNF-α was observed in the control group, which demonstrated a severe inflammatory response. Whereas, little secretion was observed in the PDMo+H_2O_2+NIR and PDMoT+H_2O_2+NIR groups, indicating few signs of inflammation or infection formation. From the Giemsa staining in Fig. 8b, it could be seen clearly that there were almost

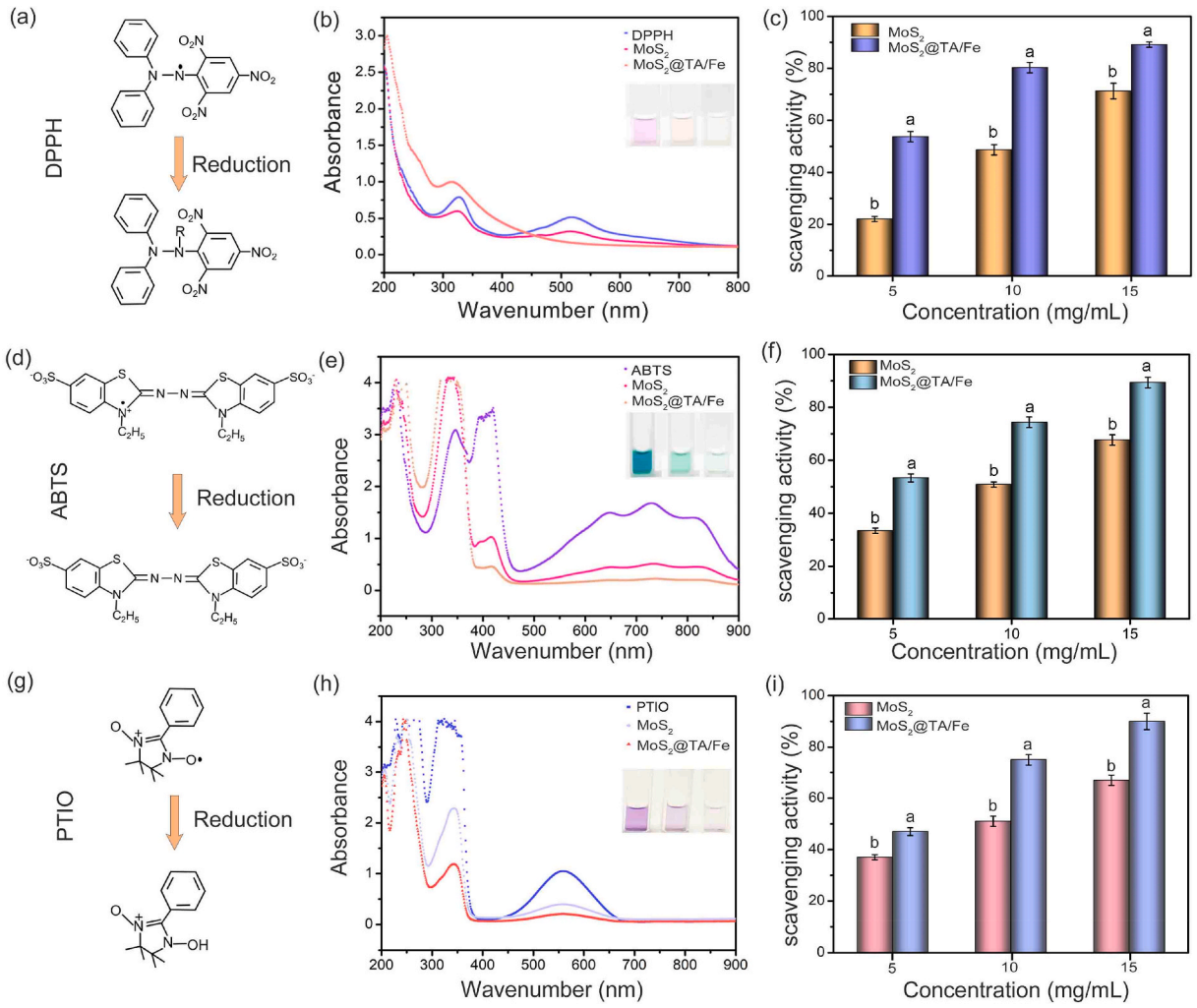

Fig. 7. Free radical scavenging ability of hydrogels. (a) Mechanism of DPPH assays. (b) DPPH assays absorbance curves and (c) scavenging ratio of hydrogels with different NSs concentration. (d) Mechanism of ABTS assays. (e) ABTS assays absorbance curves and (f) scavenging ratio of hydrogels with different NSs concentration. (g) Mechanism of PTIO assays. (h) PTIO assays absorbance curves and (i) scavenging ratio of hydrogels with different NSs concentration.

no bacteria in PDMo+H_2O_2+NIR and PDMoT+H_2O_2+NIR groups. This phenomenon was attributed to the combined efficiencies of PTT, nanozyme, and GSH loss, which all can kill microorganisms and ensure that the hydrogel had excellent antibacterial capability.

Besides preventing infection, the hydrogels presented an extraordinary wound repair and skin regeneration advantage. H&E staining results demonstrated that the wound boundary between the wound and normal tissue was clear cut and well defined at day 2. When it came to day 8, there were big differences between 14 groups, and a tiny wound could be seen in the PDMoT+H_2O_2+NIR group. Epithelium formation marks the end of the wound healing process. From Fig. 8b, there was a natural and mature epidermal layer in the PDMoT+H_2O_2+NIR group, indicating a complete wound healing. As demonstrated above, the hydrogel possessed shape-adaptivity and adhesiveness, which guaranteed a strong binding affinity and intimate integration with the irregular wound bed. Benefitting from this, the hydrogel can provide a biomimetic microenvironment for cell proliferation and migration to achieve the growth of new epidermis. Additionally, the hydrogel can promote the formation of new granulation tissue and blood vessels for tissue repair and angiogenesis because of the synergistic effects of the hydrogels, nanozyme activity, PTT therapy, O_2 supply, anti-oxidant and anti-inflammatory abilities. To further evaluate the wound healing of the hydrogels, the tissues were performed with Masson's trichrome staining (Fig. 8b). On the eighth day, the wounds of the PDMoT+H_2O_2+NIR group presented more established collagen fibres, demonstrating a better healing efficiency.

To investigate the biological mechanism of the repair process, the immunofluorescence staining of VEGF was conducted to evaluate the blood vessel density in the wound bed (Fig. 8c). From the microscale observation based on the VEGF staining, it was found that the blood vessel formation in PDMoT+H_2O_2+NIR group was more than other groups, indicating that the hydrogels can promote wound repair and skin regeneration notably.

Moreover, the immumohistochemical staining of VEGF, IL-10 and TNF-α was conducted. From Fig. S12, we can see that the expression of VEGF in the PDMoT+H_2O_2+NIR group was the highest compared to the other groups, whereas TNF-α was the lowest, which was consistent with the immunofluorescence results. In terms of the inflammatory response, IL-10 could inhibit the activation, migration and adhesion of inflammatory cells and the synthesis and release of inflammatory cytokines, thus playing an anti-inflammatory role. The IL-10 expression in the PDMoT+H_2O_2+NIR group was much higher than that in the other groups, indicating prominent anti-inflammatory ability (Fig. S12).

To assess the toxicology of hydrogels *in vivo*, H&E staining of major organs of rats, including the heart, liver, kidney, lung and spleen, was carried out at day 8 post surgery (Fig. S13). All groups showed negligible organ damage, confirming that the hydrogel would be a safe wound dressing.

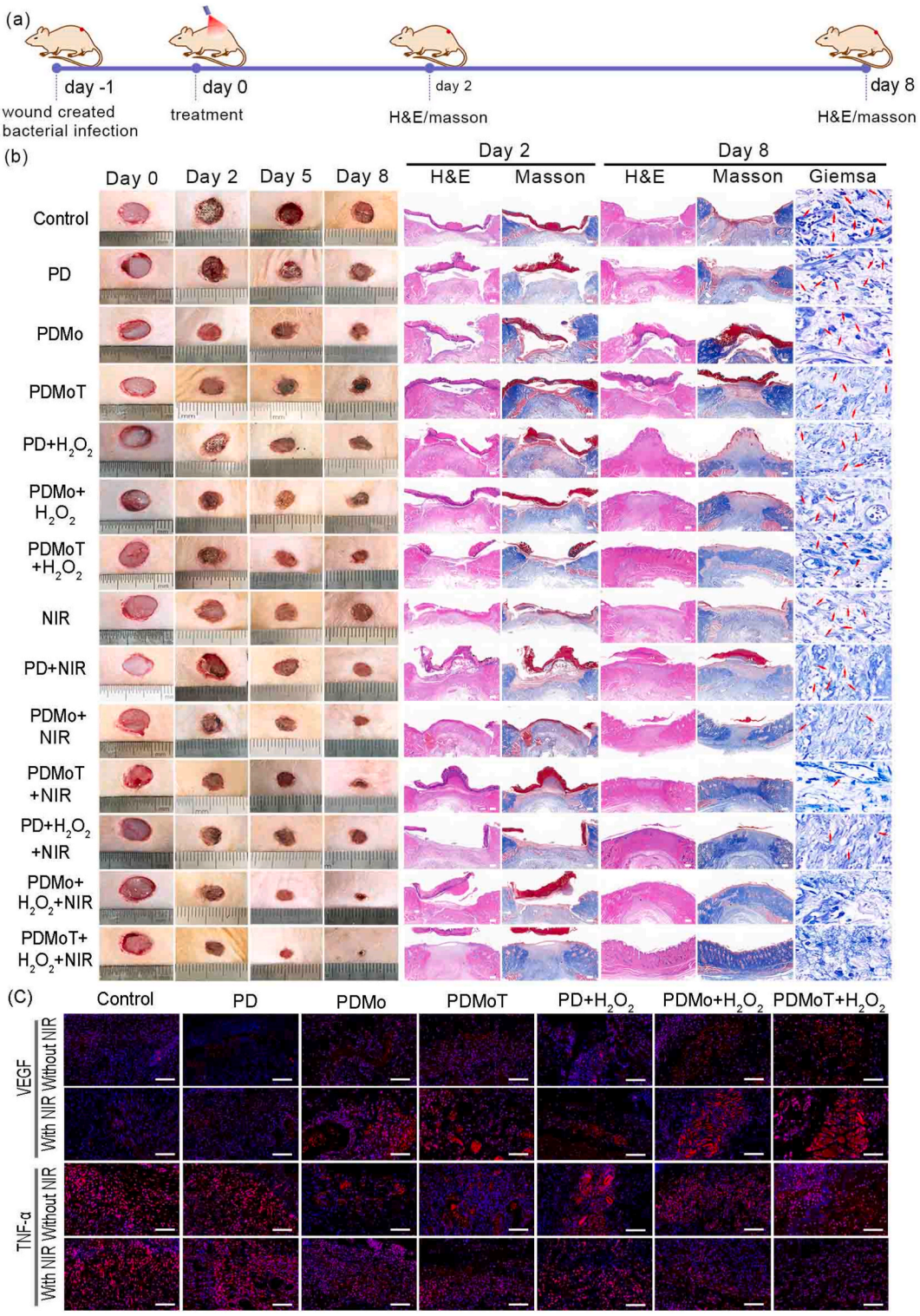

Fig. 8. (a) Schematic diagram of the *S. aureus*-infected wound model and treatment strategy. (b) Photographs of the infected wound at different days and the histologic analyses at days 2 and 8. The scale bar in the H&E and Masson staining is 200 μm. The scale bar in the Giemsa staining is 10 μm. (c) Pictures of the immunofluorescence of regenerated wound tissue on day 5 with VEGF and TNF-α. The scale bar in the histologic picture is 50 μm.

4. Conclusion

In summary, we developed a multifunctional MoS_2@TA/Fe NSs-based hydrogel for infected wound healing. MoS_2@TA/Fe NSs endowed the hydrogel with high antibacterial activity against *E. coli* and *S. aureus* due to PTT activity, POD-like activity and GSH loss, and abundant O_2 supplement benefitting from the CAT-like activity. POD-like activity was mainly on account of MoS_2 NSs, while CAT-like activity was primarily due to TA/Fe complex. Additionally, MoS_2@TA/Fe NSs gave the hydrogel with outstanding anti-oxidant ability to scavenge redundant ROS and RNS under neutral environment to maintain the balance of antioxidant systems and prevent inflammation. Moreover, TA molecules provided the hydrogels with anti-inflammatory properties to inhibit the release of inflammatory factors from macrophages. The

dynamic boron ester bonds between MoS_2@TA/Fe, PVA, Dex and borax provided the hydrogel multiple functions, including its excellent tissue-adhesive ability, fast self-healing feature, and rapid wound shape adaptivity. Furthermore, the hydrogel could promote cell proliferation *in vitro* and significantly facilitate infected wound healing by killing bacteria, reducing inflammation, supplying O_2, adjusting free radical levels, and promoting vessel growth during the wound healing cascade process. This study demonstrates the important role of MoS_2@TA/Fe nanosheets in infected wound healing, indicating that a multifunctional PDMoT hydrogel could accelerate wound healing and skin regeneration.

CRediT authorship contribution statement

Yang Li: Methodology, Validation, Formal analysis, Investigation, Data curation, Writing – original draft. **Rongzhan Fu:** Methodology, Investigation. **Zhiguang Duan:** Methodology, Software. **Chenhui Zhu:** Conceptualization, Methodology, Writing – review & editing, Project administration, Funding acquisition. **Daidi Fan:** Conceptualization, Methodology, Writing – review & editing, Project administration, Funding acquisition.

Declaration of competing interest

The authors declare that they have no known competing financial interests or personal relationships that could have appeared to influence the work reported in this paper.

Acknowledgements

This work was supported by the National Natural Science Foundation of China (grant numbers 21878247), Key Program of the National Natural Science Foundation of China (grant numbers 21838009), National Key Research and Development Program (2019YFA0905200), and Xi'an Science and Technology Project (20191422315KYPT014JC016). The authors thank Dr. J.C. Li (School of Chemical Engineering, Northwest University, Xi'an, China) for improving the manuscript during revising.

Appendix A. Supplementary data

Supplementary data to this article can be found online at https://doi.org/10.1016/j.bioactmat.2021.07.023.

References

[1] A.L. Hook, C.Y. Chang, J. Yang, S. Atkinson, R. Langer, D.G. Anderson, M. C. Davies, P. Williams, M.R. Alexander, Discovery of novel materials with broad resistance to bacterial attachment using combinatorial polymer microarrays, Adv. Mater. 25 (2013) 2542–2547.
[2] Y. Zhao, Z. Chen, Y. Chen, J. Xu, J. Li, X. Jiang, Synergy of non-antibiotic drugs and pyrimidinethiol on gold nanoparticles against superbugs, J. Am. Chem. Soc. 135 (2013) 12940–12943.
[3] V.T.H. Pham, V.K. Truong, M.D.J. Quinn, S.M. Notley, Y. Guo, V.A. Baulin, M. Al Kobaisi, R.J. Crawford, E.P. Ivanova, Graphene induces formation of pores that kill spherical and rod-shaped bacteria, ACS Nano 9 (2015) 8458–8467.
[4] G. Han, R. Ceilley, Chronic wound healing: a review of current management and treatments, Adv. Ther. 34 (2017) 599–610.
[5] M.A. Mofazzal Jahromi, P. Sahandi Zangabad, S.M. Moosavi Basri, K. Sahandi Zangabad, A. Ghamarypour, A.R. Aref, M. Karimi, M.R. Hamblin, Nanomedicine and advanced technologies for burns: preventing infection and facilitating wound healing, Adv. Drug Deliv. Rev. 123 (2018) 33–64.
[6] Z. Wang, K. Dong, Z. Liu, Y. Zhang, Z. Chen, H. Sun, J. Ren, X. Qu, Activation of biologically relevant levels of reactive oxygen species by Au/g-C_3N_4 hybrid nanozyme for bacteria killing and wound disinfection, Biomaterials 113 (2017) 145–157.
[7] J. Il Kang, K.M. Park, K.D. Park, Oxygen-generating alginate hydrogels as a bioactive acellular matrix for facilitating wound healing, J. Ind. Eng. Chem. 69 (2019) 397–404.
[8] S. Schreml, R.M. Szeimies, L. Prantl, S. Karrer, M. Landthaler, P. Babilas, Oxygen in acute and chronic wound healing, Br. J. Dermatol. 163 (2010) 257–268.
[9] Z. Yuan, C. Lin, L. Dai, Y. He, J. Hu, K. Xu, B. Tao, P. Liu, K. Cai, Near-infrared light-activatable dual-action nanoparticle combats the established biofilms of methicillin-resistant Staphylococcus aureus and its accompanying inflammation, Small (2021) 1–16, 2007522.
[10] T. Chen, Y. Chen, H.U. Rehman, Z. Chen, Z. Yang, M. Wang, H. Li, H. Liu, Ultratough, self-healing, and tissue-adhesive hydrogel for wound dressing, ACS Appl. Mater. Interfaces 10 (2018) 33523–33531.
[11] C. Hu, L. Long, J. Cao, S. Zhang, Y. Wang, Dual-crosslinked mussel-inspired smart hydrogels with enhanced antibacterial and angiogenic properties for chronic infected diabetic wound treatment via pH-responsive quick cargo release, Chem. Eng. J. 411 (2021) 128564.
[12] R. Yu, Y. Yang, J. He, M. Li, B. Guo, Novel supramolecular self-healing silk fibroin-based hydrogel via host-guest interaction as wound dressing to enhance wound healing, Chem. Eng. J. 417 (2020) 128278.
[13] B. Yang, J. Song, Y. Jiang, M. Li, J. Wei, J. Qin, W. Peng, F.L. Lasaosa, Y. He, H. Mao, J. Yang, Z. Gu, Injectable Adhesive self-healing multicross-linked double-network hydrogel facilitates full-thickness skin wound healing, ACS Appl. Mater. Interfaces 12 (2020) 57782–57797.
[14] L. Sun, Y. Huang, Z. Bian, J. Petrosino, Z. Fan, Y. Wang, K.H. Park, T. Yue, M. Schmidt, S. Galster, J. Ma, H. Zhu, M. Zhang, Sundew-Inspired adhesive hydrogels combined with adipose-derived stem cells for wound healing, ACS Appl. Mater. Interfaces 8 (2016) 2423–2434.
[15] S. Lu, X. Zhang, Z. Tang, H. Xiao, M. Zhang, K. Liu, L. Chen, L. Huang, Y. Ni, H. Wu, Mussel-inspired blue-light-activated cellulose-based adhesive hydrogel with fast gelation , rapid haemostasis and antibacterial property for wound healing, Chem. Eng. J. 417 (2021) 129329.
[16] L.G. Ding, S. Wang, B.J. Yao, F. Li, Y.A. Li, G.Y. Zhao, Y. Bin Dong, Synergistic antibacterial and anti-inflammatory effects of a drug-loaded self-standing porphyrin-COF membrane for efficient skin wound healing, Adv. Healthc. Mater. (2021) 1–12, 2001821.
[17] X. Yan, W.W. Fang, J. Xue, T.C. Sun, L. Dong, Z. Zha, H. Qian, Y.H. Song, M. Zhang, X. Gong, Y. Lu, T. He, Thermoresponsive in situ forming hydrogel with sol-gel irreversibility for effective methicillin-resistant Staphylococcus aureus infected wound healing, ACS Nano 13 (2019) 10074–10084.
[18] S. Liu, X. Liu, Y. Ren, P. Wang, Y. Pu, R. Yang, X. Wang, X. Tan, Z. Ye, V. Maurizot, B. Chi, Mussel-Inspired dual-cross-linking hyaluronic acid/ε-polylysine hydrogel with self-healing and antibacterial properties for wound healing, ACS Appl. Mater. Interfaces 12 (2020) 27876–27888.
[19] J. Xi, G. Wei, L. An, Z. Xu, Z. Xu, L. Fan, L. Gao, Copper/Carbon hybrid nanozyme: tuning catalytic activity by the copper state for antibacterial therapy, Nano Lett. 19 (2019) 7645–7654.
[20] J. Shan, X. Li, K. Yang, W. Xiu, Q. Wen, Y. Zhang, L. Yuwen, L. Weng, Z. Teng, L. Wang, Efficient bacteria killing by Cu_2WS_4 nanocrystals with enzyme-like properties and bacteria-binding ability, ACS Nano 13 (2019) 13797–13808.
[21] Y. Liu, N. Nie, H. Tang, C. Zhang, K. Chen, W. Wang, J. Liu, Effective antibacterial activity of degradable copper-doped phosphate-based glass nanozymes, ACS Appl. Mater. Interfaces 13 (2021) 11631–11645.
[22] W. Yin, J. Yu, F. Lv, L. Yan, L.R. Zheng, Z. Gu, Y. Zhao, Functionalized nano-MoS_2 with peroxidase catalytic and near-infrared photothermal activities for safe and synergetic wound antibacterial applications, ACS Nano 10 (2016) 11000–11011.
[23] M. Xu, Y. Hu, Y. Xiao, Y. Zhang, K. Sun, T. Wu, N. Lv, W. Wang, W. Ding, F. Li, B. Qiu, J. Li, Near-infrared-controlled nanoplatform exploiting photothermal promotion of peroxidase-like and OXD-like activities for potent antibacterial and anti-biofilm therapies, ACS Appl. Mater. Interfaces 12 (2020) 50260–50274.
[24] X. Li, X. Zhang, W. Zhang, L. Li, W. Gao, X. Zhang, D. Gao, Biocatalysis of MnO_2-mediated nanosystem for enhanced multimodal therapy and real-time tracking, ACS Sustain. Chem. Eng. 8 (2020) 13206–13214.
[25] M. Song, T. Liu, C. Shi, X. Zhang, X. Chen, Bioconjugated manganese dioxide nanoparticles enhance chemotherapy response by priming tumor-Associated macrophages toward M1-like phenotype and attenuating tumor hypoxia, ACS Nano 10 (2016) 633–647.
[26] S. Wang, H. Zheng, L. Zhou, F. Cheng, Z. Liu, H. Zhang, L. Wang, Q. Zhang, Nanoenzyme-reinforced injectable hydrogel for healing diabetic wounds infected with multidrug resistant bacteria, Nano Lett. 20 (2020) 5149–5158.
[27] X. Zhang, C. Zhang, Y. Yang, H. Zhang, X. Huang, R. Hang, X. Yao, Light-assisted rapid sterilization by a hydrogel incorporated with Ag_3PO_4/MoS_2 composites for efficient wound disinfection, Chem. Eng. J. 374 (2019) 596–604.
[28] X. Zhang, G. Zhang, H. Zhang, X. Liu, J. Shi, H. Shi, X. Yao, P.K. Chu, X. Zhang, A bifunctional hydrogel incorporated with CuS@MoS_2 microspheres for disinfection and improved wound healing, Chem. Eng. J. 382 (2020) 122849.
[29] B. Ma, W. Dang, Z. Yang, J. Chang, C. Wu, MoS_2 Nanoclusters-based biomaterials for disease- impaired wound therapy, Appl. Mater. Today. 20 (2020) 100735.
[30] N. Ninan, A. Forget, V.P. Shastri, N.H. Voelcker, A. Blencowe, Antibacterial and anti-inflammatory pH-responsive tannic acid-carboxylated agarose composite hydrogels for wound healing, ACS Appl. Mater. Interfaces 8 (2016) 28511–28521.
[31] B. Qiao, Y. Luo, H.B. Cheng, J. Ren, J. Cao, C. Yang, B. Liang, A. Yang, X. Yuan, J. Li, L. Deng, P. Li, H.T. Ran, L. Hao, Z. Zhou, M. Li, Y. Zhang, P.S. Timashev, X. J. Liang, Z. Wang, Artificial nanotargeted cells with stable photothermal performance for multimodal imaging-guided tumor-specific therapy, ACS Nano 14 (2020) 12652–12667.
[32] T. Liu, M. Zhang, W. Liu, X. Zeng, X. Song, X. Yang, X. Zhang, J. Feng, Metal ion/tannic acid assembly as a versatile photothermal platform in engineering multimodal nanotheranostics for advanced applications, ACS Nano 12 (2018) 3917–3927.
[33] C. Dunnill, T. Patton, J. Brennan, J. Barrett, M. Dryden, J. Cooke, D. Leaper, N. T. Georgopoulos, Reactive oxygen species (ROS) and wound healing: the functional role of ROS and emerging ROS-modulating technologies for augmentation of the healing process, Int. Wound J. 14 (2017) 89–96.

[34] J. Li, C. Zhang, H. Ma, T. Wang, Z. Guo, Y. Yang, Y. Wang, H. Ma, Modulating interfacial charge distribution of single atoms confined in molybdenum phosphosulfide heterostructures for high efficiency hydrogen evolution, Chem. Eng. J. 414 (2021) 128834.
[35] W. Wang, X. Zeng, J.H. Warner, Z. Guo, Y. Hu, Y. Zeng, J. Lu, W. Jin, S. Wang, J. Lu, Y. Zeng, Y. Xiao, Photoresponse-bias modulation of a high-performance MoS_2 photodetector with a unique vertically stacked 2H-MoS_2/1T@2H-MoS_2 structure, ACS Appl. Mater. Interfaces 12 (2020) 33325–33335.
[36] Y. Fu, L. Liu, L. Zhang, W. Wang, Highly conductive one-dimensional nanofibers: silvered electrospun silica nanofibers via poly(dopamine) functionalization, ACS Appl. Mater. Interfaces 6 (2014) 5105–5112.
[37] C. Maerten, L. Lopez, P. Lupattelli, G. Rydzek, S. Pronkin, P. Schaaf, L. Jierry, F. Boulmedais, Electrotriggered confined self-assembly of metal-polyphenol nanocoatings using a morphogenic approach, Chem. Mater. 29 (2017) 9668–9679.
[38] W. Xu, E.H. Han, Z. Wang, Effect of tannic acid on corrosion behavior of carbon steel in NaCl solution, J. Mater. Sci. Technol. 35 (2019) 64–75.
[39] D. Li, X. Xu, X. Wang, R. Li, C. Cai, T. Sun, Y. Zhao, L. Chen, J. Xu, N. Zhao, General surface modification method for nanospheres via tannic acid-Fe layer-by-layer deposition: preparation of a magnetic nanocatalyst, ACS Appl. Nano Mater. 2 (2019) 3510–3517.
[40] M.L. Lin, Q.H. Tan, J. Bin Wu, X.S. Chen, J.H. Wang, Y.H. Pan, X. Zhang, X. Cong, J. Zhang, W. Ji, P.A. Hu, K.H. Liu, P.H. Tan, Moiré phonons in twisted bilayer MoS_2, ACS Nano 12 (2018) 8770–8780.
[41] Q. Zeng, Y. Qian, Y. Huang, F. Ding, X. Qi, J. Shen, Polydopamine nanoparticle-dotted food gum hydrogel with excellent antibacterial activity and rapid shape adaptability for accelerated bacteria-infected wound healing, Bioact. Mater. 6 (2021) 2647–2657.
[42] W. Fu, X. Zhang, L. Mei, R. Zhou, W. Yin, Q. Wang, Z. Gu, Y. Zhao, Stimuli-Responsive small-on-large nanoradiosensitizer for enhanced tumor penetration and radiotherapy sensitization, ACS Nano 14 (2020) 10001–10017.
[43] L. Kou, R. Sun, S. Xiao, Y. Zheng, Z. Chen, A. Cai, H. Zheng, Q. Yao, V. Ganapathy, R. Chen, Ambidextrous approach to disrupt redox balance in tumor cells with increased ROS production and decreased GSH synthesis for cancer therapy, ACS Appl. Mater. Interfaces 11 (2019) 26722–26730.
[44] X. Wang, L. Fan, L. Cheng, Y. Sun, X. Wang, X. Zhong, Q. Shi, F. Gong, Y. Yang, Y. Ma, Z. Miao, Z. Zha, Biodegradable nickel disulfide nanozymes with GSH-depleting function for high-efficiency photothermal-catalytic antibacterial therapy, IScience 23 (2020) 101281.
[45] G. Chen, Y. Yu, X. Wu, G. Wang, J. Ren, Y. Zhao, Bioinspired multifunctional hybrid hydrogel promotes wound healing, Adv. Funct. Mater. 28 (2018) 1–10.